RESEARCH ARTICLE

Engineering 3D-Printed UHPC: Optimising Fibre Content and Printing Direction for Enhanced Mechanical Performance

Jie Wu[1], **Zhangyu Wu**[2], **Yanjie Qiao**[1], **Weiqi Dong**[1], **Rena C. Yu**[3], **Yujie Huang**[1,*] **and Hui Zhang**[1,*]

[1] School of Environment and Safety Engineering, North University of China, Taiyuan 030051, China
[2] Jiangsu Key Laboratory of Construction Materials, School of Materials Science and Engineering, Southeast University, Nanjing 211189, China
[3] ETS de Ingenieros de Caminos, Canales y Puertos, Universidad de Castilla-La Mancha, Ciudad Real 13071, Spain

Abstract

3D-printed ultra-high-performance concrete (3DP-UHPC), which combines high strength, high toughness, and construction flexibility, provides a solution to the reinforcement difficulty of conventional printed concrete. However, the layer-by-layer printing process induces pronounced anisotropy in compressive and flexural properties, which remains a key challenge for engineering applications. We used X-ray computed tomography (X-CT) to quantitatively analyse the internal pores and to reveal the orientation and distribution of steel fibres in 3DP-UHPC. Splitting tensile tests showed that the interlayer splitting tensile strength is approximately 49.3% lower than the conventional splitting tensile strength, and increasing fibre content has a limited strengthening effect. Analysis of the compressive anisotropy index λ_c indicates that, at $V_f = 0\%$, anisotropy is mainly influenced by weak interlayer interfaces and pore distribution. Linear fitting shows that a small fibre addition ($V_f \leq 1.28\%$) reduces compressive anisotropy, whereas higher V_f leads to an increase in λ_c due to fibre orientation. For the flexural anisotropy index λ_f, interstrip interfaces and pores dominate at $V_f = 0\%$ and 0.5%, while fibre distribution governs λ_f when $V_f \geq 1.0\%$, with an increase exceeding 60%. Within $V_f = 0\% - 2.0\%$, λ_c remains higher than λ_f, indicating relatively stable compressive performance. These results provide experimental evidence for optimising the compressive and flexural performance of 3DP-UHPC components in engineering applications.

Keywords: 3D printed ultra-high-performance concrete (3DP-UHPC), mechanical anisotropy, compressive and flexural behaviour, steel fibre orientation, multi-scale damage evolution.

Submitted: 05 January 2026
Accepted: 08 February 2026
Published: 24 February 2026

Vol. 2, **No.** 1, 2026.
10.62762/JAMR.2026.817012

***Corresponding authors:**
✉ Yujie Huang
mpcyujie@nuc.edu.cn
✉ Hui Zhang
zhangh@nuc.edu.cn

Citation
Wu, J., Wu, Z., Qiao, Y., Dong, W., Yu, R. C., Huang, Y., & Zhang, H. (2026). Engineering 3D-Printed UHPC: Optimising Fibre Content and Printing Direction for Enhanced Mechanical Performance. *Journal of Advanced Materials Research*, 2(1), 40–54.

1 Introduction

In recent years, the integration of concrete additive manufacturing technology with ultra-high-performance concrete (UHPC) has promoted the development of a novel cementitious material, namely 3D printed ultra-high-performance concrete (3DP-UHPC) [1–4]. This material not only inherits the high strength and high toughness characteristics of UHPC, but also benefits from the advantages of 3D printing technology, including reduced construction time, decreased formwork usage, enhanced flexibility in structural fabrication, and lower labour demand [5–9]. In addition, owing to the incorporation of steel fibres, 3DP-UHPC shows the potential to partially replace the reliance on conventional reinforcement in traditional 3D printed concrete elements [4], thereby providing a feasible technological pathway for the integrated and automated printing of high-strength and high-toughness structural components [10].

Despite the aforementioned advantages arising from the combination of these two technologies, the layer-by-layer deposition nature of 3D printing leads to pronounced mechanical anisotropy in 3DP-UHPC. For example, with respect to compressive performance, Yang et al. [11] reported that the compressive strength in the $z-$direction was 189% and 88% higher than those in the $x-$ and $y-$directions, respectively, while the $y-$direction strength exceeded that in the $x-$direction by 54%. Shahzad et al. [12] observed increases of 15% and 7% in the $z-$direction relative to the $x-$ and $y-$directions, respectively, and reported that the $y-$direction strength was 7% higher than that in the $x-$direction. Yao et al. [5] pointed out that directional differences in compressive strength persist over a fibre volume fraction range of 0.5% to 2.0%. Jia et al. [13] found comparable compressive strengths in the $z-$ and $y-$directions, whereas the $x-$direction strength was approximately 24% lower. In contrast, Arunothayan et al. [14] reported similar strengths in the $y-$ and $z-$directions, with the $x-$direction strength being about 12% higher than both.

These studies demonstrate that the compressive strength of 3DP-UHPC exhibits clear anisotropy across different printing directions. Although most experiments indicate that the compressive strength in the $z-$ or $y-$direction is higher than that in the $x-$direction, the magnitude of anisotropy varies considerably among the reported results, and the relative strength ranking among directions is not always consistent. Such discrepancies are likely attributable to differences in fibre content, specimen dimensions, and printing parameters.

With regard to flexural performance, Yang et al. [11] measured a 258% increase in flexural strength in the $z-$direction compared with the $x-$direction. Shahzad et al. [12] reported that the $z-$direction strength was 94% higher than that in the $x-$direction. Jia et al. [13] observed that the flexural strength in the $y-$direction exceeded that in the $x-$direction by 145%. Arunothayan et al. [14] found that the flexural strength in the $z-$direction was approximately three times that in the $x-$direction. Overall, flexural strength is generally weakest in the $x-$direction. These findings indicate that the flexural behaviour of 3DP-UHPC also exhibits pronounced anisotropy. Owing to the elongated rectangular geometry of flexural specimens, flexural performance is more sensitive to the arrangement and stacking direction of the printed strip, which further influences the strength measured in different directions.

The above studies demonstrate that both the magnitude of anisotropy and the direction exhibiting superior performance vary among different investigations. Such mechanical anisotropy may lead to an imbalance in structural performance under service loading. For example, flexural members subjected to bending along the $x-$direction are more susceptible to through-cracking or excessive deflection, thereby posing a potential risk to structural safety. Consequently, a systematic analysis of the factors influencing mechanical anisotropy in 3DP-UHPC, together with clarification of the mechanisms responsible for the differences between compressive and flexural anisotropy, is of significant importance.

In addition, interlayer interfaces formed during the layer-by-layer deposition of 3DP-UHPC constitute weak regions within printed specimens, and their mechanical properties directly affect load-bearing capacity. Previous studies have shown that the interlayer bonding strength of printed specimens is approximately 67% of the splitting tensile strength of cast specimens with the same mix design, resulting in a reduction in compressive and tensile or flexural strength [15]. Luo et al. [16] found that shorter printing time intervals between layers lead to denser interface structures, whereas longer intervals increase porosity and weaken the interlayer interface. Yang et al. [17] further indicated that hot-water curing can contribute to the healing of interlayer defects. Existing studies have mainly focused on processing

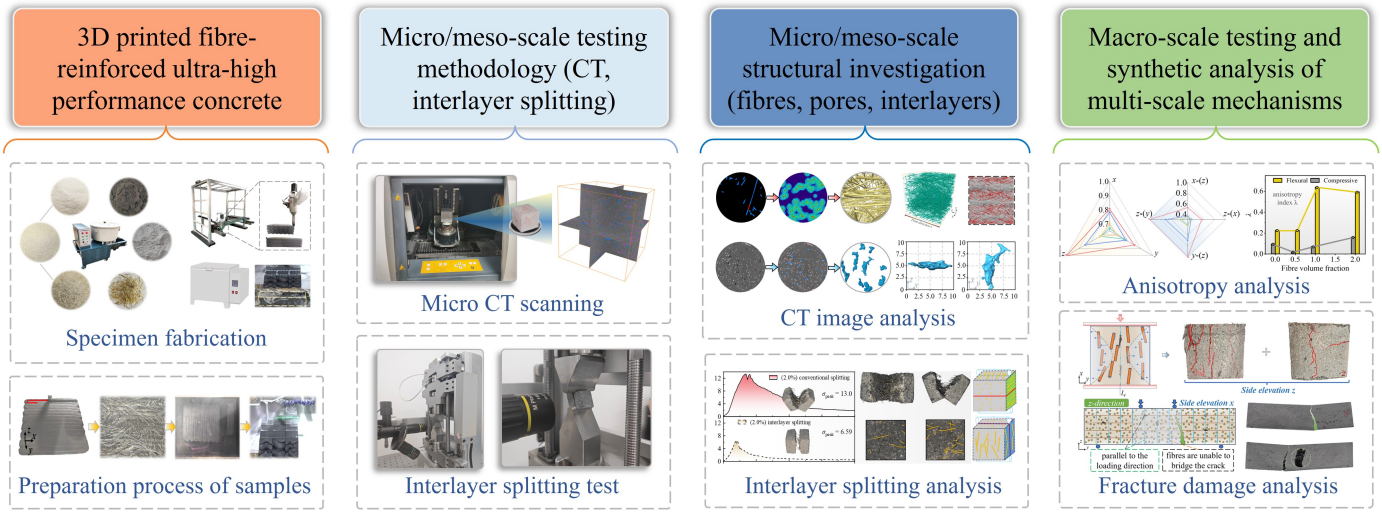

Figure 1. Flowchart of the multi-scale fracture analysis methodology for 3DP-UHPC.

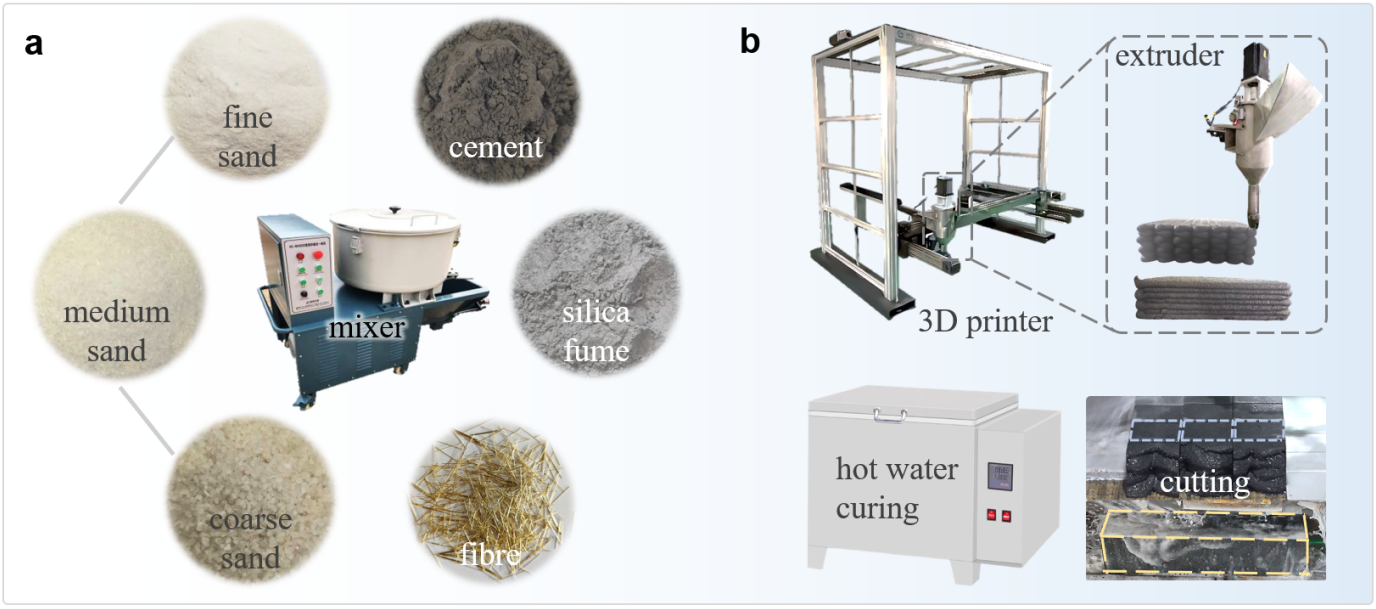

Figure 2. Schematic of the specimen fabrication process for 3D printing UHPC. (a) Material preparation and mixing. (b) Printing and specimen fabrication.

parameters and have not yet examined in depth the multi-scale effects of interlayer pore structure, fibre distribution and fibre-bridging effects on the evolution of interfacial strength, as well as on material damage and fracture behaviour [18], under different steel fibre contents. Moreover, the intrinsic relationship and underlying mechanisms between compressive and flexural anisotropy have not been systematically elucidated.

To address these gaps, this study prepared 3DP-UHPC specimens with steel fibre volume fractions of 0%, 0.5%, 1.0% and 2.0%. Uniaxial compression, four-point bending and interlayer splitting tensile tests were conducted. X-ray computed tomography [19] was employed to quantify pore number and morphological characteristics and to reveal fibre orientation and distribution. Combined with post-failure fracture surface observations, the anisotropic evolution of compressive and flexural performance was systematically investigated and compared, elucidating micro/meso-structural effects on compressive and flexural anisotropy. The technical workflow is illustrated in Figure 1.

2 Results

2.1 3D printing of UHPC based on close packing

Figure 2 illustrates the preparation procedure of the 3D printed specimens. Figure 2(a) presents the composition of the raw materials. The binder consisted of 52.5-grade ordinary Portland cement (OPC) and

silica fume with a specific surface area of 6339 m^2/kg. The aggregates comprised three grades of quartz sand with different particle sizes. The proportions of the five solid constituents were determined according to particle size distribution and dense packing theory. In addition, nano-calcium carbonate (NCC) with a particle size ranging from 10 to 100 nm was incorporated to fill micropores, and a melamine-based high-range water-reducing admixture was added to improve flowability. Copper-coated steel fibres with a diameter of 0.2 mm and a length of 13 mm were used as the reinforcing fibres.

The mixing procedure was as follows. All dry materials were first premixed for 3 min, after which the superplasticiser solution was added and mixing continued for a further 5 min. Steel fibres were then slowly introduced, and mixing was maintained until uniform dispersion was achieved. Finally, mixing was continued for an additional 10 min to ensure thorough homogenisation. The steel fibre volume fractions were set at 0%, 0.5%, 1.0% and 2.0%. The 3D printing system was a gantry-type steel frame structure, as shown in Figure 2(b), equipped with a nozzle of 30 mm in diameter. After printing, the specimens were covered with plastic film and cured for 24 h, followed by curing in a hot-water bath at 90°C for 72 h, resulting in a total curing period of 4 d. Upon completion of curing, the printed elements were cut into cubic specimens with a side length of 70.7 mm for compressive tests, prismatic specimens measuring 100 × 100 × 400 mm for flexural tests, and cubic specimens for splitting test with a side length of 20 mm.

2.2 Computed tomography (CT) test

Figure 3 illustrates the CT data processing procedure for 3DP-UHPC. To characterise the internal microstructural features after printing, a cubic specimen with a side length of 70.7 mm, a steel fibre volume fraction of 1.0%, and containing six to eight printed strips was selected (Figure 3(a)). The specimen was scanned using an RMCT4000 micro-focus X-ray CT system operated at 190 kV and 200 μA, with a spatial resolution of 50 μm.

Image preprocessing was conducted using Avizo software, as shown in Figure 3(b). A Gaussian filter was applied to reduce slice noise, and an effective region with a side length of 54.95 mm was cropped to minimise the influence of X-ray scattering on image quality near the specimen boundaries [14]. Based on the fact that greyscale intensity reflects material density, with steel fibres appearing brightest, followed by the cementitious matrix and pores appearing darkest, greyscale-based threshold segmentation was performed on the CT images (8-bit, 0–255) to achieve three-phase identification of pores, matrix and steel fibres. The Line-Probe method was first employed to determine the preliminary threshold ranges, as illustrated in Figure 3(c), namely pores (0–60), matrix (61–144) and steel fibres (145–255). Subsequently, a sensitivity analysis of pore volume fraction with respect to the greyscale threshold was carried out (Figure 3(d)). Each data point represents the pore volume fraction calculated from CT segmentation at a specific greyscale threshold value. The results were fitted using a fourth-order polynomial. The optimal pore threshold range of 0–55 was determined from the minimum-slope point where the second derivative equals zero, corresponding to a calculated porosity of 2.24%. Given the distinctly higher greyscale intensity of steel fibres relative to the matrix and pores, the initially adopted fibre threshold range (145–255) serves primarily for 3D visualisation and for preliminary fibre localisation in X-Fibre [4]. The quantitative reconstruction of fibre orientation and spatial distribution, however, is performed accurately and efficiently by X-Fibre using cylinder correlation and trace correlation, rather than relying solely on simple greyscale thresholding. Therefore, unlike pore volume fraction, the fibre threshold does not require additional sensitivity analysis, as X-Fibre robustly identifies fibres even within the initial greyscale range.

Figure 4 presents the micro/meso-structural distribution characteristics of pores and steel fibres in 3DP-UHPC. As shown in Figure 4(a-b), the maximum pore diameter in the printed specimens reaches 3200 μm, while small pores account for a large proportion. Pores with diameters of 0–250 μm constitute 67.2% of the total, and those within the range of 0–1000 μm account for as much as 99.3%, with an average equivalent diameter of only 264 μm. This value is lower than the average pore diameters of 700 μm and 380 μm reported by Zhang et al. [20] and Ríos et al. [21] for cast UHPC, which can be attributed to the effective compaction and expulsion of pores during the printing process. A total of 37 pores larger than 2000 μm were identified, all of which were interlayer and interstrip pores. Unlike the ellipsoidal pores typically observed in cast specimens, these interlayer and interstrip pores are influenced by strip dragging during extrusion, resulting in an average sphericity of only 0.59. Consequently, they exhibit irregular shapes, with several pores showing

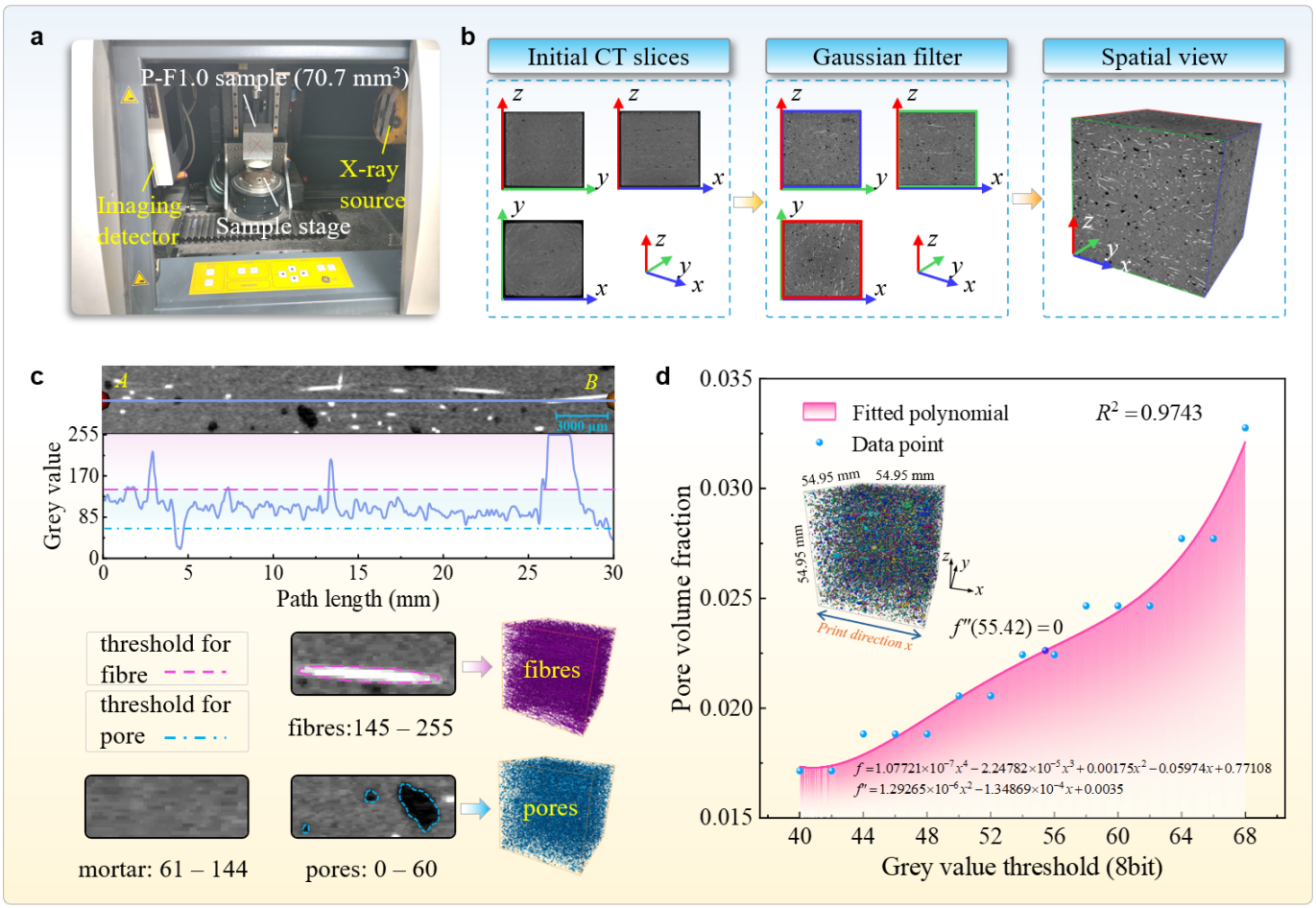

Figure 3. CT data processing and three-phase thresholding of 3DP-UHPC. (a) CT scanning of a 70.7 mm cube specimen. (b) Pre-processing and denoising of the CT slices. (c) Initial threshold determination using the line-probe method, with grey value ranges of 0–60 for pores, 61–144 for mortar, and 145–255 for fibres. (d) Sensitivity analysis of pore volume fraction based on fourth-order polynomial fitting, from which the optimal pore threshold (0–55) is identified and used for 3D visualisation.

pronounced elongation along the printing direction (L_x).

Figure 4(c) illustrates the three-dimensional rendering of steel fibres and the definition of the dual angular parameters (θ and φ) for individual fibres, where θ ranges from 0° to 90° and φ from 0° to 360°. Fibre orientation was classified into three levels, namely low, medium and high. Figure 4(d) quantifies the proportion of fibres within different angular ranges and highlights their spatial distribution in red using a perspective view. The results indicate that fibres with a high degree of orientation in terms of θ account for 65.2%, whereas fibres with a low degree of orientation in terms of φ account for 42.8%, demonstrating a clear difference between the two angular distributions. This discrepancy is mainly attributed to the spatial confinement (height or thickness) imposed by the printed strips, which constrains fibre alignment during the printing process. The quantitative analysis clearly shows the directional distribution characteristics of the fibres.

2.3 Interlayer splitting test

Both interlayer and conventional splitting tensile tests (with loading applied at non-interlayer positions) were conducted using cubic 3DP-UHPC specimens with a side length of 20 mm. The tests were performed on a MINI-MTS10000 loading system [4] under a displacement-controlled loading rate of 0.1 μm/s. The experimental results are presented in Figure 5. The splitting tensile strength of the interlayer specimens is consistently lower than that of the conventional specimens and decreases with decreasing steel fibre volume fraction in the range of 0–2.0%. This behaviour is attributed to the limited number of fibres bridging the interlayer interface in the interlayer specimens, resulting in weaker fibre-bridging effects compared with the conventional specimens. Fracture surface observations (side view) further indicate that a large

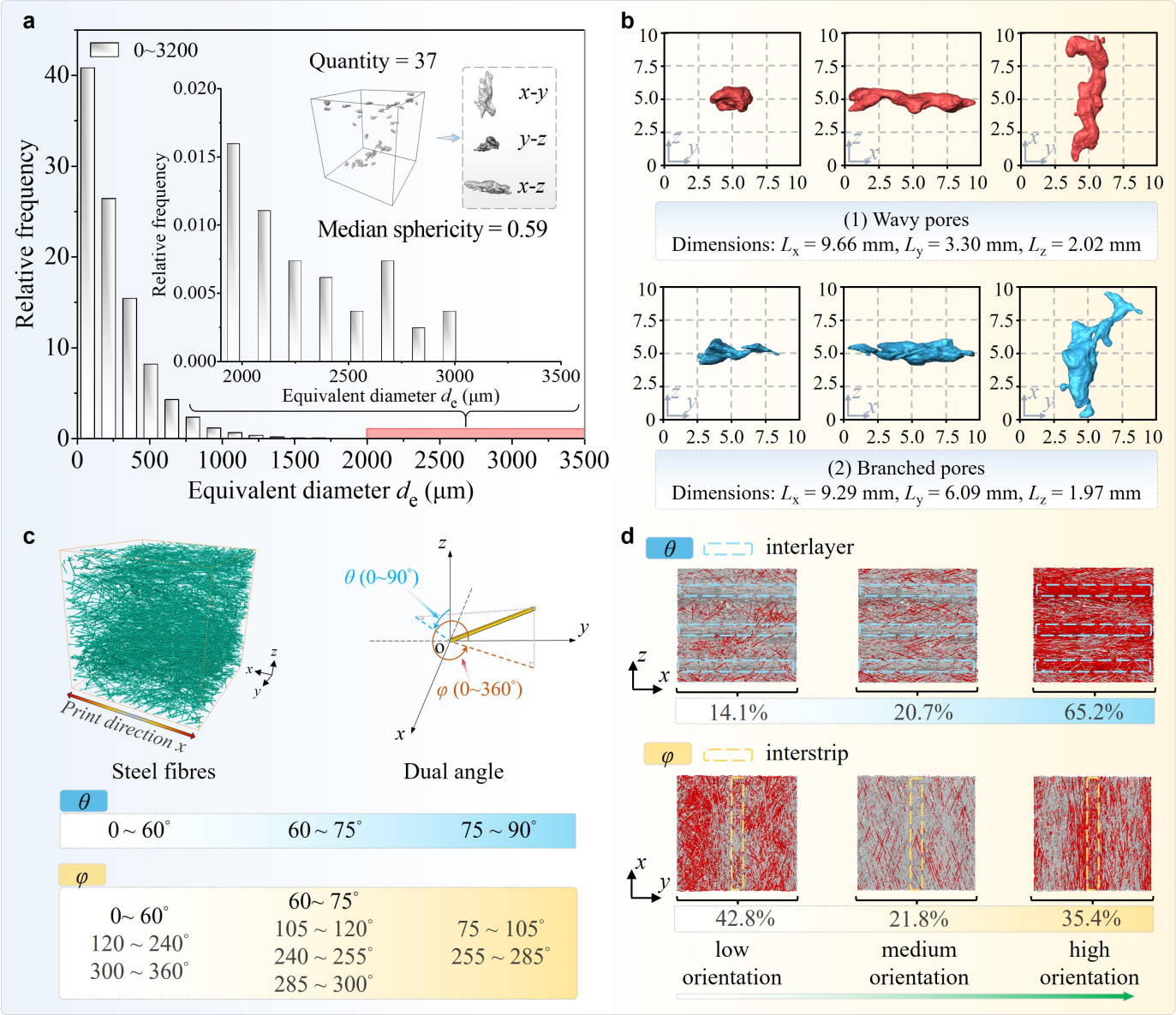

Figure 4. Quantification and characterisation of pore and fibre micro/meso-structures in 3D-UHPC. (a) Distribution of equivalent pore diameters over the range of 0–3200 μm, with an inset highlighting the 2000–3200 μm range, together with 3D renderings of 37 irregular pores (median sphericity = 0.59). (b) 3D morphologies and characteristic size parameters of two types of interlayer- and interstrip-type pores within the 2000–3200 μm range. (c) 3D renderings of steel fibres and definitions of the dual orientation angles θ and φ, which are divided into three intervals, with orientation intensity increasing from low to high. (d) Statistical distributions of fibre orientations, where θ is evaluated in the $x-y$ plane and φ in the $x-z$ plane; regions with high orientation intensity are highlighted in red.

number of oriented fibres bridge the crack in the conventional splitting specimens, thereby providing substantial crack-bridging resistance.

Regarding the splitting tensile behaviour of interlayer specimens, a further analysis of the influence of fibre volume fraction indicates that, as the steel fibre content increases from 0% to 2.0%, the peak stress rises from 4.3 MPa to 6.59 MPa, corresponding to an increase of approximately 53.3%. Meanwhile, the descending branch of the stress–displacement curves becomes progressively gentler, indicating that compared with the enhancement in interlayer splitting tensile strength, higher fibre content leads to a more pronounced improvement in toughness. This is because, as evidenced by the fracture characteristics (Figure 5), an increase in fibre content results in a greater number of fibres appearing in the interlayer region, thereby enhancing interlayer toughness. At a fibre volume fraction of 2.0%, the highest number of fibres is observed within the interlayer region, and these fibres exhibit twisted and disordered configurations after specimen failure, as shown in the magnified view.

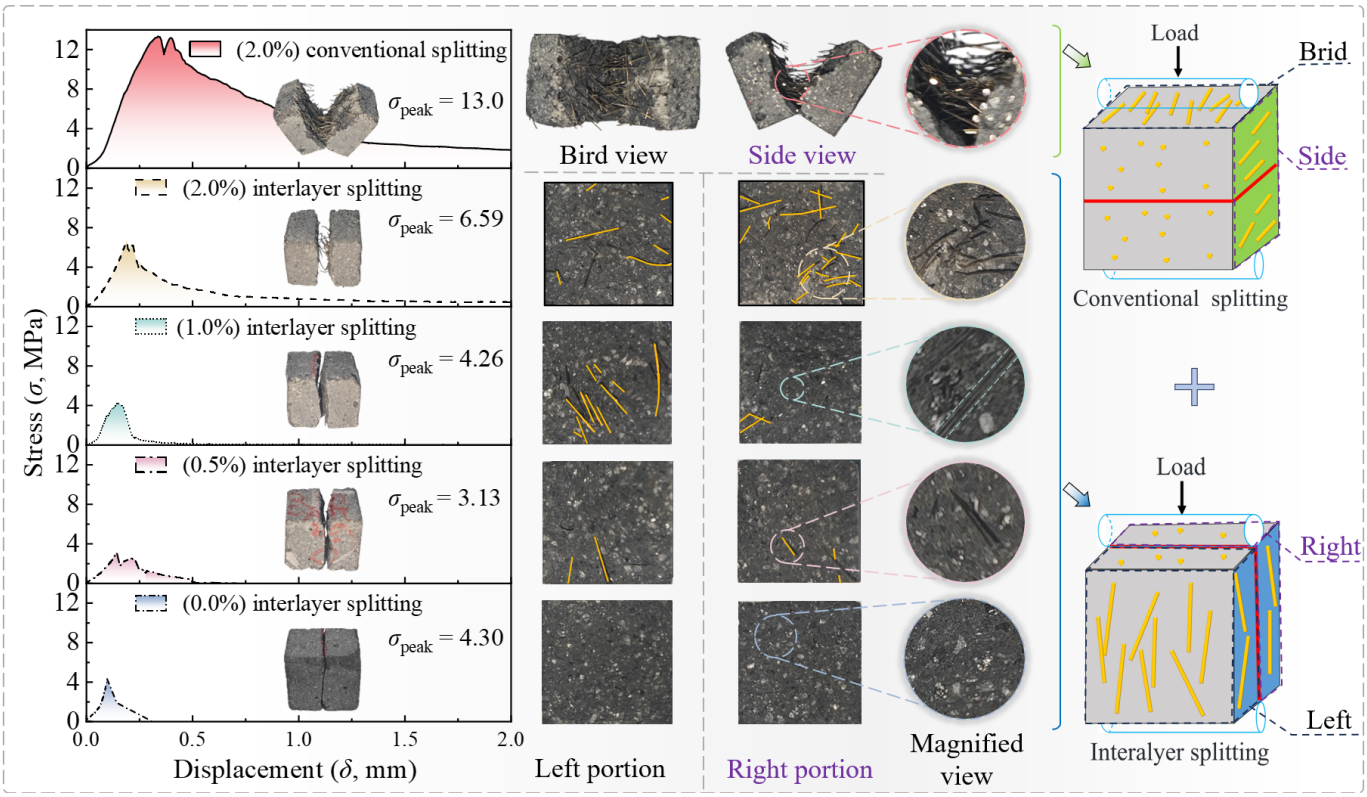

Figure 5. Stress–displacement curves and failure modes of 3DP-UHPC under conventional and interlayer splitting tests with different steel fibre volume fractions.

Such configurations increase the energy dissipation associated with fibre pull-out.

2.4 Mechanical behaviour and anisotropy

To investigate the anisotropic mechanical behaviour of 3DP-UHPC under different loading directions, uniaxial compression and four-point bending tests were carried out using a WAW-1000 electro-hydraulic servo universal testing machine at a loading rate of 0.1 mm/min. As illustrated in Figure 6(a), the compressive tests were performed along three loading directions, namely x, y and z, with a loading rate of 0.06 mm/min. For the flexural tests, four loading configurations were considered: x-(z), z-(x), y-(z) and z-(y). For instance, the specimens are denoted as "x-(z)", where x indicates the loading axis and (z) (in parentheses) represents the plane indicated by the arrow in the Figure 6.

Figure 6(b) presents stacked bar charts of strength results obtained under the same loading direction for different steel fibre volume fractions. The results show that the compressive strength follows the order $z > y > x$, whereas the flexural strength follows the sequence z-$(y) > y$-$(z) > z$-$(x) > x$-(z). The radar plots in Figure 6(c) further illustrate these trends: for compressive strength, increasing steel fibre content causes the vertices of the triangular plot to shift markedly towards the z-direction, indicating that the greatest enhancement in compressive strength occurs along this direction. For flexural strength, an increase in fibre content results in two vertices of the quadrilateral plot shifting prominently towards the lower-left region, indicating that the flexural strength in the z-(y) and y-(z) directions increases most significantly, while the remaining directions exhibit comparatively smaller improvements.

To quantitatively characterise the anisotropy of the mechanical properties of 3DP-UHPC, an anisotropy index λ was introduced, where λ_c and λ_f correspond to the anisotropy of compressive and flexural strength, respectively. The compressive anisotropy index λ_c is defined as follows [4]:

$$\lambda_c = \frac{\sqrt{(f_x - f_{Ave})^2 + (f_y - f_{Ave})^2 + (f_z - f_{Ave})^2}}{f_{Ave}} \quad (1)$$

where f_{Ave} denotes the average compressive strength of the printed concrete specimens, and f_x, f_y and f_z represent the compressive strengths measured along the x-, y- and z-directions, respectively.

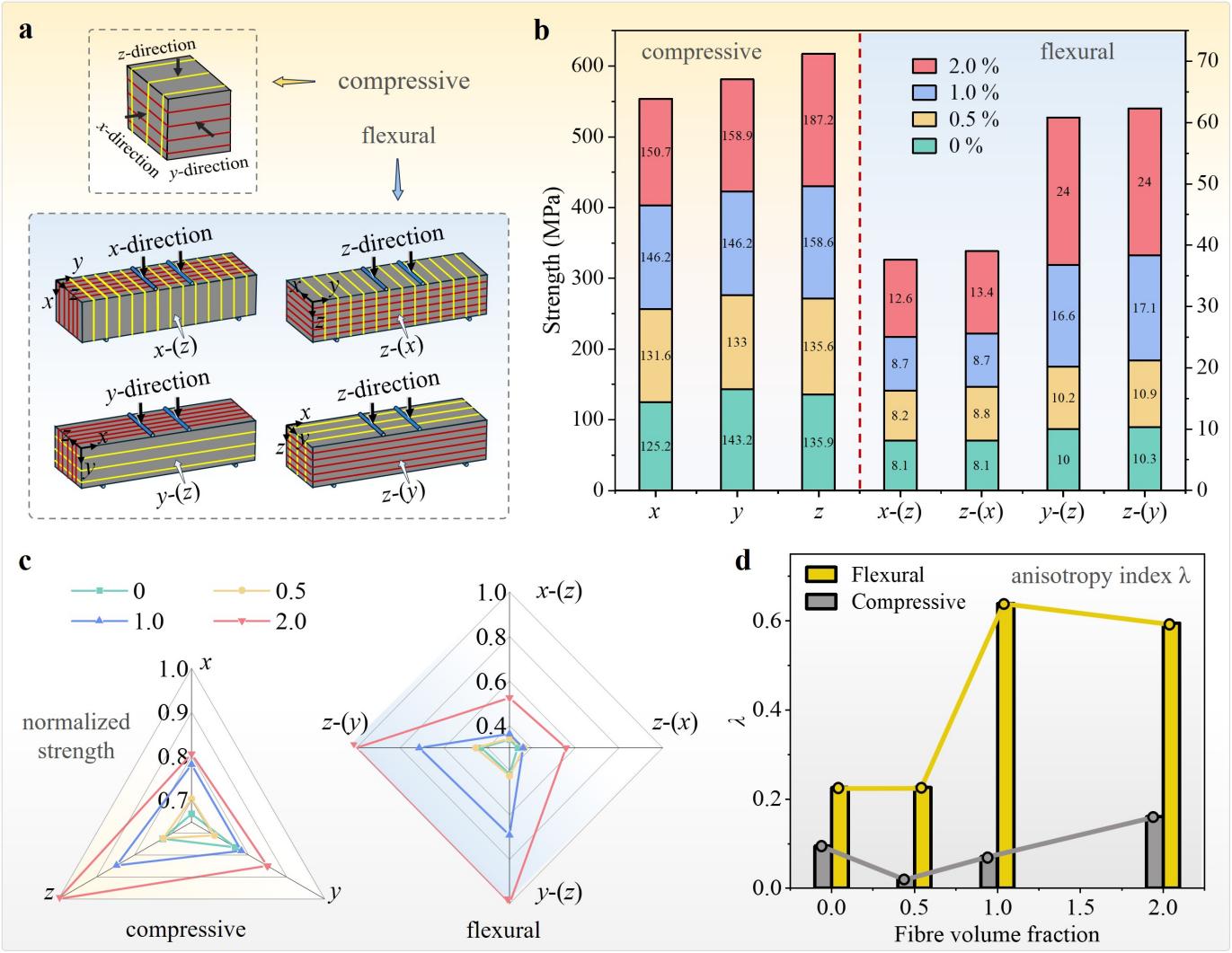

Figure 6. Compressive and flexural mechanical properties of 3DP-UHPC and their anisotropic characteristics. (a) Specimen orientations and loading configurations for compression and flexural tests. Compressive loads were applied along the $x-$, $y-$, and $z-$directions; for flexural tests, the notation $x-(z)$ denotes loading along the $x-$direction with the layer orientation in the $z-$direction. (b) Combined bar chart showing compressive and flexural strengths of 3DP-UHPC at different steel fibre volume fractions under different loading directions. (c) Normalised radar charts illustrating the anisotropy of compressive and flexural strengths. (d) Anisotropy index (λ) of compressive and flexural performance as a function of steel fibre volume fraction.

The flexural anisotropy index, λ_f, is defined as follows:

$$\lambda_f = \frac{\sqrt{\left(f_{x-(z)} - f_{Ave}\right)^2 + \left(f_{z-(x)} - f_{Ave}\right)^2 + \left(f_{y-(z)} - f_{Ave}\right)^2 + \left(f_{z-(y)} - f_{Ave}\right)^2}}{f_{Ave}} \quad (2)$$

where f_{Ave} denotes the average flexural strength of the printed concrete specimens, and $f_{x-(z)}$, $f_{z-(x)}$, $f_{y-(z)}$ and $f_{z-(y)}$ correspond to the flexural strengths obtained under the four loading configurations of x-(z), z-(x), y-(z) and z-(y), respectively.

Tables 1, 2 and Figure 6(d) present the values of the compressive and flexural anisotropy indices, λ_c and λ_f, together with their mean values and standard deviations. With respect to the compressive anisotropy index λ_c, it can be observed that λ_c initially decreases and subsequently increases with increasing steel fibre volume fraction. In the absence of fibres, λ_c reaches 0.095, which is higher than the values obtained at fibre contents of 0.5% and 1.0%. This behaviour can be attributed to the fact that, without steel fibres, the anisotropy of 3DP-UHPC is mainly governed by weak interlayer interfaces, as illustrated in Figure 5, and by the distribution of interlayer pores, as shown in Figure 4.

When the fibre volume fraction V_f is 0.5%, λ_c reaches its minimum value of 0.022 among the tested fibre volume fractions, indicating a relatively balanced

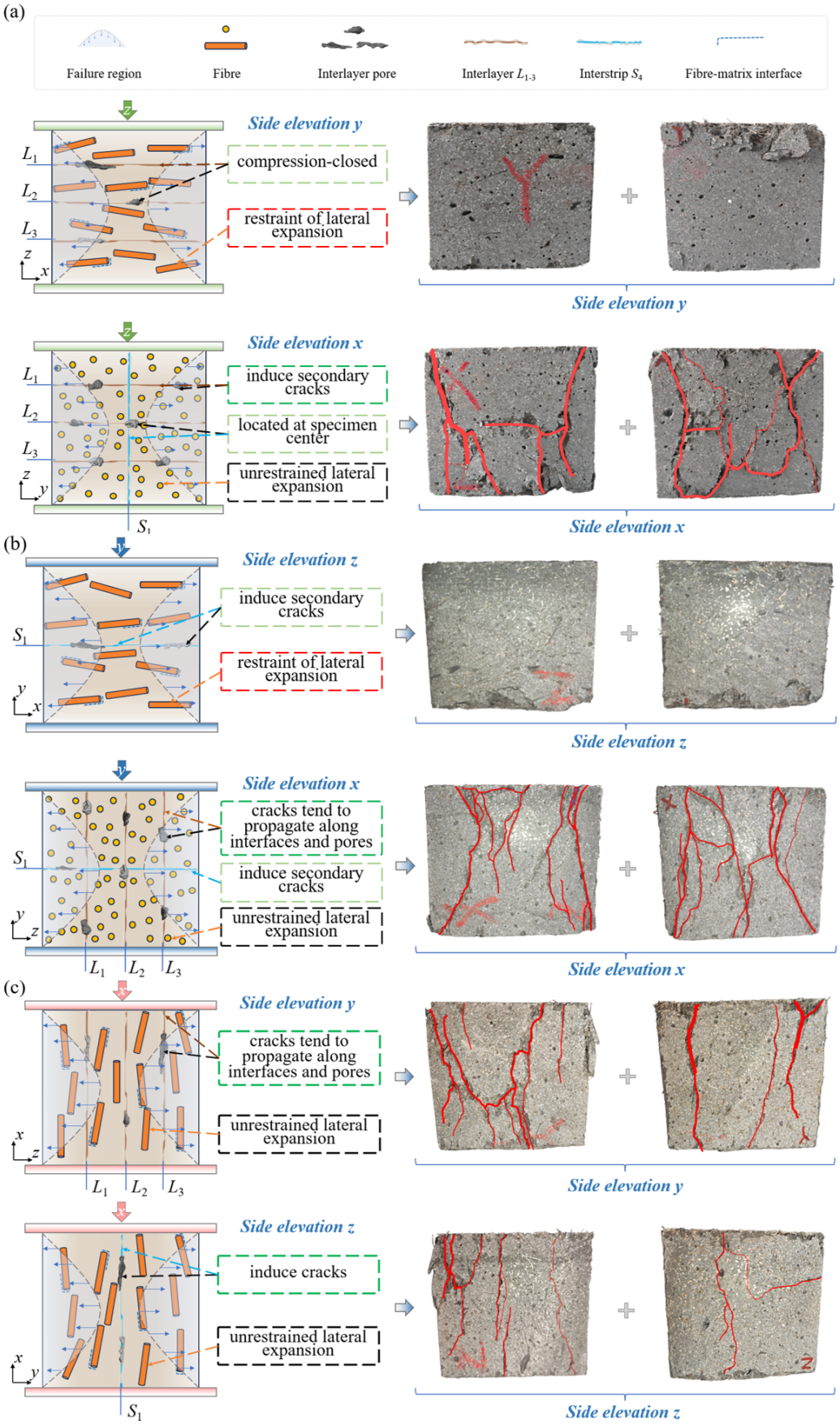

Figure 7. Failure mechanisms of specimens under compression along different loading directions (z, y, and x): effects of interlayer/interstrip interfaces, interlayer/interstrip porosity, and steel fibre orientation.

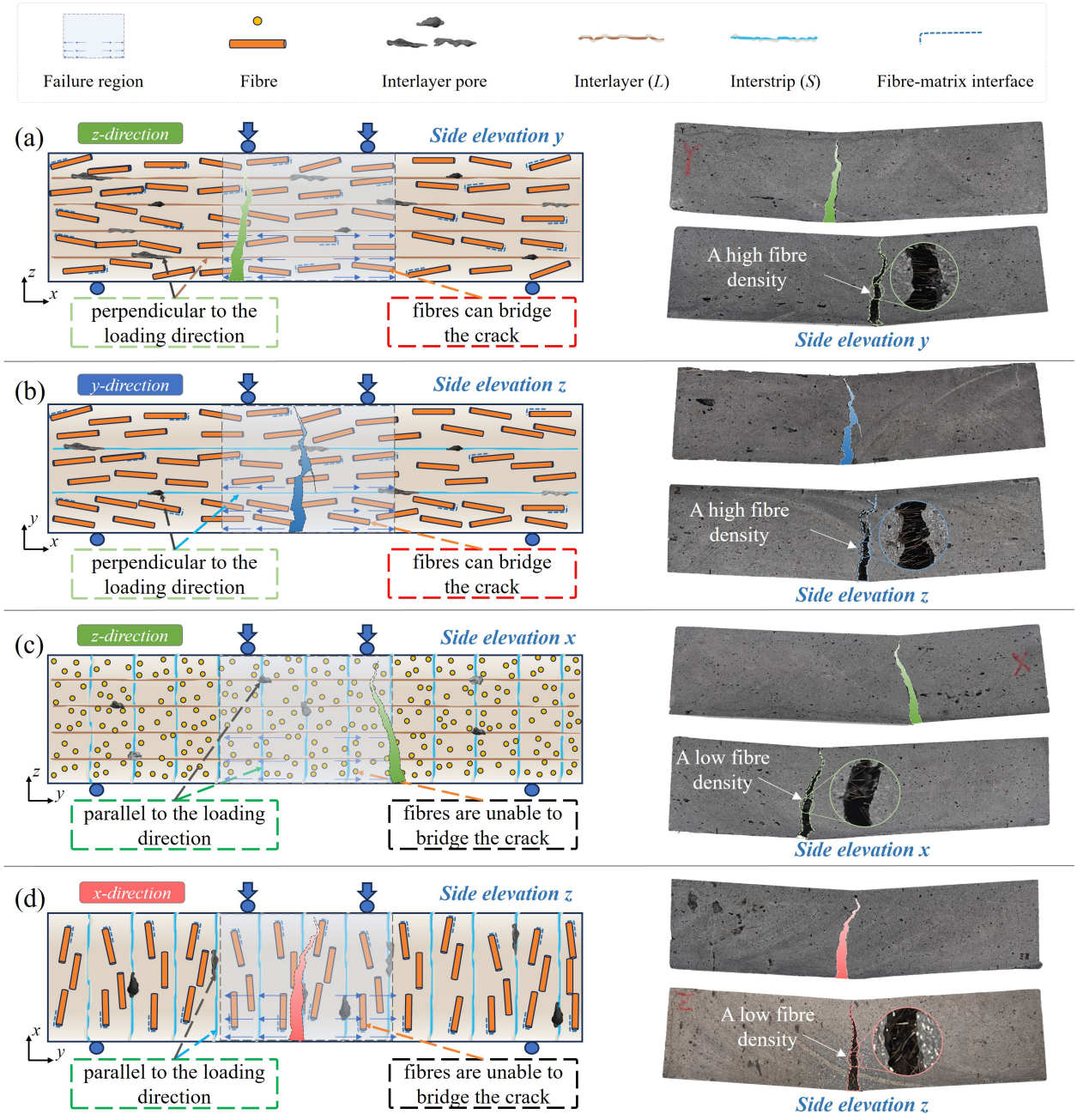

Figure 8. Failure mechanisms of four-point flexural specimens under different loading directions $(z-(y), y-(z), x-(z), z-(x))$: effects of interlayer/interstrip interfaces, pores, and steel fibre orientation.

compressive strength distribution among the three loading directions in this study. Within the range of $V_f = 0.5\%$ to 2.0%, λ_c increases linearly with increasing V_f, and the fitted relationship can be expressed as

$$\lambda_c = 0.09229 \times V_f - 0.023 \quad (3)$$

The near-linear rise in λ_c with V_f reflects a progressive amplification of direction-dependent reinforcement as the number of preferentially aligned fibres increases during extrusion, thereby widening the disparity in compressive strength among the three loading directions. It should be noted that the observed linear trend is supported by experimental data only within the fibre volume fraction range of $V_f = 0.5\% - 2.0\%$. Behaviour at lower $(V_f < 0.5\%)$ or higher $(V_f > 2.0\%)$ fibre contents may deviate from linearity and requires further verification. At very low fibre contents $(V_f < 0.5\%)$, reduced fibre bridging and toughening would lead to decreased ductility, a more brittle, matrix–dominated failure mode, and even if anisotropy were further reduced, such an "approximately isotropic" state would not necessarily correspond to an optimal mechanical

Table 1. Compressive strength and anisotropy index λ_c of 3DP-UHPC.

Fibre volume fraction (%)	Compressive strength (MPa)			Measured anisotropy λ_c	Mean of λ_c	Standard deviation of λ_c
	x	y	z			
0	125	143	136	0.095	0.087	0.058
0.5	132	133	136	0.022		
1.0	146	146	159	0.071		
2.0	151	159	187	0.161		

Table 2. Flexural strength and anisotropy index λ_f of 3DP-UHPC.

Fibre volume fraction (%)	Flexural strength (MPa)				Measured anisotropy λ_f	Mean of λ_f	Standard deviation of λ_f
	x-(z)	z-(x)	y-(z)	z-(y)			
0	8.1	8.1	10	10.3	0.226	0.421	0.227
0.5	8.2	8.8	10.2	10.9	0.226		
1.0	8.7	8.7	16.6	17.1	0.639		
2.0	12.6	13.4	24.0	24.0	0.595		

performance for engineering applications. Conversely, fibre contents exceeding 2.0% are often limited by printability constraints, including reduced extrusion stability and increased risk of nozzle blockage.

Based on the fitted equation, a V_f value of 1.28% is obtained when λ_c corresponds to the case without fibre addition ($\lambda_c = 0.095$). Therefore, within the range of V_f from 0% to 1.28%, fibre incorporation is beneficial for reducing the anisotropy of compressive strength. This can be attributed to the fact that the addition of steel fibres enhances the cementitious matrix and simultaneously improves interlayer mechanical performance, as shown in Figure 5. As a result, stress distribution within the specimens becomes more uniform, which mitigates the adverse effects of weak interlayer interfaces and leads to a reduction in compressive strength anisotropy. When $V_f > 1.28\%$, the high fibre content combined with the directional distribution characteristics of fibres increases the anisotropy of compressive strength; meanwhile, the interlayer strength is not substantially enhanced at high fibre contents (Figure 5), such that weak interfaces remain prone to stress concentration and crack initiation, resulting in a further increase in the compressive anisotropy index.

For the flexural anisotropy index λ_f, the influence of fibre content is more pronounced. At low fibre contents ($V_f = 0\%$ and 0.5%), λ_f remains constant at 0.226, indicating limited fibre-bridging effects and suggesting that anisotropy is mainly governed by weak interlayer and interstrip interfaces and interlayer porosity. When the fibre content increases to 1.0%, λ_f rises sharply to 0.639, representing an increase of 183%, at which point flexural anisotropy becomes dominated by fibre orientation. At a fibre volume fraction of 2.0%, λ_f decreases, which is associated with the enhancement of interlayer splitting tensile strength at higher fibre contents (Figure 5).

A comparison between λ_c and λ_f shows that λ_f is consistently greater than λ_c over the fibre volume fraction range of 0% to 2.0%, as illustrated in Figure 6(d). This can be attributed to the fact that, under loading in the x-(z) and z-(x) configurations (Figure 6(a)), cracks preferentially initiate and propagate within the interlayer and interstrip regions, while the addition of fibres provides only a limited enhancement of the interlayer/interstrip interface strength (Figure 5). In contrast, under y-(z) and z-(y) loading, the oriented fibres effectively impede crack propagation, reducing the influence of the interlayer and interstrip regions and thereby resulting in a marked improvement in flexural strength. Consequently, the strength differences between these loading configurations remain substantial, leading to a relatively high value of λ_f. As shown in Tables 1 and 2, both the mean value and the standard deviation of the flexural anisotropy index are much larger than those of the compressive anisotropy index, indicating that compressive strength in 3DP-UHPC is more stable than flexural strength.

2.5 Synergistic compressive–flexural mechanism of 3DP-UHPC at micro/meso-scale

Significant differences in crack initiation and propagation are observed under different loading directions. Figures 7 and 8 illustrate the micro/meso-scale surface characteristics of

3DP-UHPC specimens subjected to compression and flexure, respectively, including schematic representations of steel fibres, pores, and interlayer and interstrip interfaces, together with the damage patterns after failure. To intuitively reflect the roles of steel fibres, interlayer interfaces, and pores in local load-carrying capacity or crack resistance, coloured annotations are adopted in the explanatory boxes: red indicates enhancement, dark green indicates pronounced weakening, light green indicates slight weakening, and black indicates negligible influence.

Figure 7(a-c) present the lateral views of compressive failure characteristics under loading in the x, y, and z directions, respectively, as analysed below:

1. Loading in the z direction (Figure 7(a)): On the $y-$side surface, transversely aligned, line-shaped steel fibres oriented perpendicular to the loading direction provide effective crack-bridging, significantly suppressing compression-induced lateral expansion and crack initiation. Meanwhile, the interlayer interfaces are mainly subjected to compressive stress and are therefore difficult to open, resulting only in slight surface spalling. In contrast, fibres on the $x-$side surface appear as discrete points, offering limited bridging capacity and insufficient restraint against lateral expansion and crack growth. Consequently, initial cracks preferentially initiate at the corner regions on both sides and subsequently propagate towards the interlayer (L_2) and interstrip (S_1) regions, forming secondary cracks.

2. Loading in the y direction (Figure 7(b)): The $z-$side surface is similarly characterised by transversely aligned fibres, and its damage pattern closely resembles that of the $y-$side surface under the $z-$direction loading (first row of Figure 7(a)). On the $x-$side surface, fibres exhibit a point-like distribution with relatively weak bridging effects, while interlayer (L_{1-3}) interfaces and associated pores readily form preferential paths for major crack propagation, thereby reducing the overall integrity of the specimen.

3. Loading in the x direction (Figure 7(c)): On the $y-$side surface, fibres are aligned parallel to the loading direction, resulting in limited crack-bridging capability and an inability to effectively restrain lateral expansion-induced cracking. In addition, interlayer (L_{1-3}) interfaces and pores further weaken the load-bearing capacity, leading to the development of numerous vertical cracks concentrated on both sides of the specimen. On the $z-$side surface, the presence of weak interstrip (S_1) interfaces in the central region combined with porosity promotes pronounced cracking in the middle zone, resulting in poor overall structural integrity.

Figure 8 presents the lateral views of flexural failure characteristics of the specimens under four loading configurations: $z-(y)$, $y-(z)$, $x-(z)$ and $z-(x)$. The failure mechanisms are analysed as follows:

1. Loading in the $z-(y)$ direction (Figure 8(a)): On the $y-$side surface, steel fibres are oriented perpendicular to the loading direction and appear as transversely aligned, line-shaped features, providing effective crack-bridging and confinement. A large number of fibres remain across the crack opening, which restrains crack widening and propagation. The interlayer weak interfaces are also perpendicular to the loading direction and therefore have a limited influence on crack development.

2. Loading in the $y-(z)$ direction (Figure 8(b)): On the $z-$side surface, the steel fibres are likewise oriented perpendicular to the loading direction. Consequently, the damage pattern is similar to that observed under $z-(y)$ loading.

3. Loading in the $z-(x)$ direction (Figure 8c): On the $x-$side surface, steel fibres are oriented perpendicular to the loading direction but are distributed in a point-like manner within the plane, resulting in relatively weak crack-bridging and confinement. The interstrip interfaces are parallel to the loading direction and act as the primary pathways for crack propagation, causing the crack location to deviate from the mid-span region.

4. Loading in the $x-(z)$ direction (Figure 8(d)). On the $z-$side surface, steel fibres are aligned parallel to the loading direction and appear as vertically oriented, line-shaped features, providing limited bridging capacity; correspondingly, fewer fibres are observed in the crack region. The interstrip interfaces are parallel to the loading direction and serve as the dominant channels for crack propagation.

3 Discussion

These results provide valuable references for determining the steel fibre content in 3DP-UHPC for

engineering applications. The observed anisotropy in 3DP-UHPC is fundamentally governed by the process-induced alignment and distribution of fibres. For components primarily under compression, where the design objective is to reduce anisotropy and achieve a more uniform strength profile, a steel fibre volume fraction in the range of 0.5% to 1.28% is recommended. This dosage supplies adequate fibre to improve ductility and microcrack control without severely accentuating the directional variations intrinsic to the layered manufacturing process. Where maximising load-bearing capacity takes precedence and some strength anisotropy is acceptable, higher fibre contents may be considered. Given the characteristically high compressive strength of 3DP-UHPC in all loading orientations, the practical influence of this anisotropy on failure risk is often mitigated, as long as the induced stresses remain beneath the respective directional strength limits.

In the case of flexural members, the interplay between fibre content and anisotropy is more critical. While low fibre contents from 0% to 0.5% correlate with lower flexural anisotropy, they typically yield insufficient flexural capacity. Significantly increasing the steel fibre content enhances flexural performance markedly by improving crack bridging, but it also intensifies anisotropy due to the more pronounced directional alignment of fibres. Consequently, achieving an optimal balance is key. From an engineering design standpoint, optimising the printing path offers a strategic method to harness the material's inherent strengths. By deliberately aligning critical tensile zones with the material's stronger directions, such as perpendicular to the deposition layers or parallel to the printing travel, the beneficial effect of fibre alignment can be exploited. This approach allows for the use of higher fibre dosages to secure enhanced flexural strength while concurrently managing anisotropy through intelligent design.

4 Conclusion

Based on macroscopic mechanical tests, interlayer splitting tensile tests, and multi-scale X-ray CT characterisation, this study comparatively investigates the evolution and underlying mechanisms of compressive and flexural anisotropy in 3DP-UHPC. The main findings can be summarised as follows:

1. The interlayer splitting tensile strength of 3DP-UHPC is approximately 49.3% lower than that of conventional splitting tensile strength. Increasing the steel fibre volume fraction from 0% to 2.0% raises the interlayer strength from 4.3 MPa to 6.59 MPa, indicating that steel fibres contribute to enhancing interlayer resistance and improving fracture toughness, thereby alleviating brittle failure.

2. The compressive anisotropy index (λ_c) initially decreases and then increases with fibre content. A minimum value of 0.022 is observed at $V_f = 0.5\%$, while λ_c increases linearly for $V_f = 0.5\% - 2.0\%$. The results suggest that fibre addition below 1.28% mitigates compressive anisotropy by strengthening the matrix and interlayer regions, whereas higher contents promote fibre orientation-induced anisotropy.

3. The flexural anisotropy index (λ_f) is more sensitive to fibre content. At low fibre contents (0%–0.5%), λ_f remains at 0.226 and is mainly governed by interlayer interfaces and pores. When V_f increases to 1.0%, λ_f rises markedly to 0.639, implying a transition to fibre-orientation-dominated behaviour.

4. Within the investigated fibre range, flexural anisotropy consistently exceeds compressive anisotropy, suggesting that the compressive response of 3DP-UHPC is relatively stable across loading directions, while flexural behaviour is more strongly influenced by loading orientation and effective fibre bridging.

This study establishes a framework for optimising the mechanical performance of 3DP-UHPC. To advance this framework, future research should prioritise three interconnected avenues: the influence of fibre type and geometry on reinforcement mechanics, the effects of key printing parameters on microstructural evolution, and the development of integrated multi-scale models for performance prediction. At the modelling level, it remains crucial to advance efficient micro/meso-scale numerical approaches capable of explicitly resolving fibre–matrix interactions, as demonstrated in [22]. These aspects are essential for both improving fine-scale mechanical characterisation and enabling robust, component-level predictions through reliable upscaling.

Data Availability Statement

Data will be made available on request.

Funding

This work was supported by the National Natural Science Foundation of China under Grant 52578336 and the Young Elite Scientist Sponsorship Program of China Association for Science and Technology under Grant YESS20240332.

Conflicts of Interest

The authors declare no conflicts of interest.

AI Use Statement

The authors declare that no generative AI was used in the preparation of this manuscript.

Ethical Approval and Consent to Participate

Not applicable.

References

[1] Yang, S., Lan, T., Sun, Z., Xu, M., Wang, M., & Feng, Y. (2022). A predictive model to determine tensile strength and fracture toughness of 3D printed fiber reinforced concrete loaded in different directions. *Theoretical and Applied Fracture Mechanics, 119*, 103309. [CrossRef]

[2] Bai, G., Wang, L., Wang, F., & Ma, G. (2023). Assessing printing synergism in a dual 3D printing system for ultra-high performance concrete in-process reinforced cementitious composite. *Additive Manufacturing, 61*, 103338. [CrossRef]

[3] Yu, S., Sanjayan, J., & Du, H. (2022). Effects of cement mortar characteristics on aggregate-bed 3D concrete printing. *Additive Manufacturing, 58*, 103024. [CrossRef]

[4] Zhang, H., Wu, J., Huang, B. T., Yu, R. C., Xia, M., Sanjayan, J. G., & Huang, Y. J. (2025). Cross-scale mechanisms of anisotropy in 3D-printed Ultra-High-Performance Concrete (UHPC). *Additive Manufacturing, 114*, 105014. [CrossRef]

[5] Yao, Y., Zhang, J., Sun, Y., Pi, Y., Wang, J., & Lu, C. (2024). Mechanical properties and failure mechanism of 3D printing ultra-high performance concrete. *Construction and Building Materials, 447*, 138108. [CrossRef]

[6] Liu, H., Liu, C., Bai, G., Wu, Y., He, C., Zhang, R., & Wang, Y. (2022). Influence of pore defects on the hardened properties of 3D printed concrete with coarse aggregate. *Additive Manufacturing, 55*, 102843. [CrossRef]

[7] Yang, Y., Wu, C., Liu, Z., & Zhang, H. (2022). 3D-printing ultra-high performance fiber-reinforced concrete under triaxial confining loads. *Additive Manufacturing, 50*, 102568. [CrossRef]

[8] Geng, S. B., Zhang, C., Zhang, H., Hai, L., Huang, B. T., Han, Y. S., ... & Huang, Y. J. (2025). Upcycling coal gangue coarse aggregates into 3D printed concrete: Multi-scale mechanisms of fracture behaviour. *Cement and Concrete Composites, 164*, 106275. [CrossRef]

[9] Nguyen-Van, V., Li, S., Liu, J., Nguyen, K., & Tran, P. (2023). Modelling of 3D concrete printing process: A perspective on material and structural simulations. *Additive manufacturing, 61*, 103333. [CrossRef]

[10] Sun, X., Gao, C., & Wang, H. (2021). Bond performance between BFRP bars and 3D printed concrete. *Construction and Building Materials, 269*, 121325. [CrossRef]

[11] Yang, Y., Wu, C., Liu, Z., Wang, H., & Ren, Q. (2022). Mechanical anisotropy of ultra-high performance fibre-reinforced concrete for 3D printing. *Cement and Concrete Composites, 125*, 104310. [CrossRef]

[12] Shahzad, Q., Abbas, N., Akbar, M., Sabi, E., Thomas, B. S., & Arshid, M. U. (2024). Influence of print speed and nozzle diameter on the fiber alignment in 3D printed ultra-high-performance concrete. *Frontiers in Materials, 11*, 1355647. [CrossRef]

[13] Jia, Z., Kong, L., Jia, L., Ma, L., Chen, Y., & Zhang, Y. (2024). Printability and mechanical properties of 3D printing ultra-high performance concrete incorporating limestone powder. *Construction and Building Materials, 426*, 136195. [CrossRef]

[14] Arunothayan, A. R., Nematollahi, B., Ranade, R., Bong, S. H., Sanjayan, J. G., & Khayat, K. H. (2021). Fiber orientation effects on ultra-high performance concrete formed by 3D printing. *Cement and Concrete Research, 143*, 106384. [CrossRef]

[15] Lee, Y. J., Lee, S. H., Kim, J. H., Jeong, H., Han, S. J., & Kim, K. S. (2024). Interlayer bond strength of 3D printed concrete members with ultra high performance concrete (UHPC) mix. *Buildings, 14*(7), 2060. [CrossRef]

[16] Luo, S., Lin, Q., Xu, W., & Wang, D. (2023). Effects of interval time and interfacial agents on the mechanical characteristics of ultra-high toughnessnn cementitious composites under 3D-printed technology. *Construction and Building Materials, 374*, 130936. [CrossRef]

[17] Yang, Y., Zhang, C., Liu, Z., Dong, L., Yang, T., Zhao, Q., & Wu, C. (2024). Effect of hydration process on the interlayer bond tensile mechanical properties of ultra-high performance concrete for 3D printing. *Construction and Building Materials, 451*, 138902. [CrossRef]

[18] Zhang, H., Huang, B. T., Li, Q. H., Wang, Q. M., Hong, C. K., & Xu, S. L. (2025). Tensile fracture behavior and notch-insensitive mechanism of Strain-Hardening Cementitious Composites (SHCC) with recycled fine aggregates. *Cement and Concrete Composites*, 106281. [CrossRef]

[19] Huang, B. T., Zhang, Z. L., Xi, H., Zhang, T., Chen, M., Wei, J. H., ... & Xu, L. Y. (2025). Strain-Hardening

Ultra-High-Performance Concrete (SH-UHPC) with hybrid steel and polyethylene fibers: Enhanced tensile ductility at subzero temperatures. *Theoretical and Applied Fracture Mechanics, 139*, 104987. [CrossRef]

[20] Zhang, X., Yang, Z., Pang, M., Yao, Y., Li, Q. M., & Marrow, T. J. (2021). Ex−situ micro X-ray computed tomography tests and image-based simulation of UHPFRC beams under bending. *Cement and Concrete Composites, 123*, 104216. [CrossRef]

[21] Rios, J. D., Cifuentes, H., Leiva, C., & Seitl, S. (2019). Analysis of the mechanical and fracture behavior of heated ultra-high-performance fiber-reinforced concrete by X-ray computed tomography. *Cement and Concrete Research, 119*, 77-88. [CrossRef]

[22] Zhang, H., Huang, Y. J., Xu, S. L., Hu, X. J., & Zheng, Z. S. (2023). 3D cohesive fracture of heterogeneous CA-UHPC: a mesoscale investigation. *International Journal of Mechanical Sciences, 249*, 108270. [CrossRef]

Jie Wu is a Master's student at the School of Environment and Safety Engineering in North University of China. His research focuses on the mechanical properties and multi-scale mechanisms of 3D-printed UHPC materials. He has been awarded the Excellent Speech at the 5th International Conference on 3D Printing Concrete Materials and Structures. (Email: jiewuxh@163.com)

Zhangyu Wu is an associate professor at the School of Materials Science and Engineering in Southeast University, China. He obtained his PhD degree in Nanjing University of Aeronautics and Astronautics, China. His research focuses on cutting-edge fields including bionic superhydrophobic concrete and cement-based photothermal interface metamaterials. He is committed to addressing material challenges in island and reef engineering construction, such as the development of high-strength concrete using coral aggregates and seawater, with the aim of advancing durable and environment-adaptable construction materials. (Email: wuzy@seu.edu.cn)

Yanjie Qiao is a Master's student at the School of Environment and Safety Engineering in North University of China. His research is dedicated to green and low-carbon ultra-high-performance concrete materials and structures, with an emphasis on developing eco-friendly formulations and optimising structural performance. (Email: qyjiee@163.com)

Weiqi Dong is a Master's student at the School of Environment and Safety Engineering in North University of China. His research focuses on advancing 3D printing technologies for geopolymer concrete, aiming to enhance both printability and mechanical performance within low-carbon material systems. (Email: dongweiqi4@163.com)

Rena C. Yu is a full professor in Continuum Mechanics at the Civil Engineering School in the University of Castilla-La Mancha, Spain. She earned her Bachelor of Science in Aeronautics at Beijing University of Aeronautics and Astronautics (BUAA) in 1994, her Master in 1997 and her PhD in 2001 in Aeronautics in the California Institute of Technology (Caltech), USA. Her research focus is on experimental and computational fracture and fatigue damage in quasi-brittle materials, leveraging both finite element and meshfree methods. She is a member of the Congress Committee for IUTAM (International Union for Theoretical and Applied Mechanics) for 2024-2028 and the vice president for the Spanish Society on Theoretical and Applied Mechanics. (Email: Chengxiang.Yu@uclm.es)

Yujie Huang is an associate professor at the School of Environment and Safety Engineering, North University of China. He received his BSc from Central South University and PhD from Zhejiang University. His research encompasses 3D printing of high-performance composites and the development of advanced numerical methods. His work on in-situ CT experiments and fracture simulations has 500+ citations for a single publication. He has been the PI of seven projects, including the National Natural Science Foundation of China (General Program). He serves as an Executive Guest Editor for Theoretical and Applied Fracture Mechanics. He was awarded Second Prize of the Natural Science Award of Zhejiang Province, First Prize of Excellent Engineering Design Award of Zhejiang Province, among others. (Email: mpcyujie@nuc.edu.cn)

Hui Zhang is a professor at the School of Environment and Safety Engineering, North University of China. She received his BSc from Central South University and PhD from Zhejiang University. She leads the Smart Resilient & Low-Carbon Materials Laboratory in North University of China. Her research focuses on high-strength, high-toughness cementitious materials and innovative structural designs. She has been the PI of over ten competitive projects, including: the National Natural Science Foundation of China Project, the Shanxi Provincial Major S&T Program, and the Shanxi Provincial Ten-Billion-Yuan Project for S&T Innovation. She was selected for the Young Elite Scientist Sponsorship Program of the China Association for Science and Technology (2024) and recognised as an Outstanding Young Talent of Shanxi Province, China (2025). (Email: zhangh@nuc.edu.cn)